

304

**The Prediction of Dynamic Recrystallization and Grain
Size of 304 Stainless Steel during Hot Deformation**

2001 2

ABSTRACT	
.....	
List of Tables and Photographs	
List of Figures	
1.	1
1.1	1
1.2	2
1.3	3
2. 가	4
2.1	5
2.2	5
2.3	6
2.4	6
Figures	8
3.	10
3.1	10
3.2	11

4.	13
4.1	13
4.2	14
4.3	14
Tables	16
Photos and Figures	17
5.	24
5.1	24
5.1.1	24
5.1.2	27
5.2	31
Photos and Figures	34
6.	48
	50

**The Prediction of Dynamic Recrystallization
and Grain Size of 304 Stainless Steel during
Hot Deformation**

Young - Pyo Kwon

Department of Mechanical Engineering Graduate School.

Korea Maritime University

ABSTRACT

The flow stresses of 304 stainless steel during hot forming process were determined by conducting hot compression tests at the range of 1273 K 1423 K and 0.05 /s 2.0/s as these are typical temperature and strain rate in hot forging operation. In the material Dynamic recrystallization was found to be the major softening mechanism with this conditions as previous studies. Based on the observed phenomena, a constitutive model of flow stress was assumed as a function of strain, strain rate, temperature. In the constitutive model, the effects of strain hardening and

dynamic recrystallization were taken into consideration. A finite element method connected to constitutive model was performed to predict the dynamic recrystallization behaviors and also stress-strain curves in hot compression of 304 stainless steel.

c	:	(Specific heat) (N/mm · s · K ⁴)
C, k, m, m'	:	
d_{dyn}	:	(Dynamic Recrystallized grain size)
\bar{D}	:	(Mean grain size)
h	:	(N/mm · s · K)
h_{lub}	:	(N/mm · s · K)
K	:	(Penalty Function)
K_1	:	(Thermal Conductivity)
n	:	(Strain rate sensitivity)
n, n_i	:	
q_α	:	
Q	:	(Activation Energy)
S_f, S_v	:	가
T, T_i	:	
X_{dyn}	:	(Dynamic Recrystallization Volume Fraction)
Z	:	Zener-Hollomon Parameter
Δt	:	
$\Delta\sigma$:	
ε_c	:	
ε_p	:	
$\bar{\varepsilon}$:	(Effective Strain)

$\dot{\bar{\epsilon}}$:	(Effective Strain Rate)
$\dot{\epsilon}_{ij}$:	(Strain Rate Tensor)
ρ	:	(Mass Density) (kg/mm^3)
σ_e	:	가
σ_s	:	
$\bar{\sigma}$:	(Effective Stress)
σ_{ij}'	:	(Deviatoric Stress Tensor)

List of Tables and Photographs

Tables

Table 1 Chemical composition of stainless 304 and mechanical property

Table 2 The condition of process parameters for FE-simulation

Photographs

Photo 1 Testing equipment (Thermecmaster)

Photo 2 Microstructure of 50% compressing at 1000 and $\dot{\varepsilon} = 0.05 \text{ s}^{-1}$

Photo 3 Microstructure of 50% compressing at 1050 and $\dot{\varepsilon} = 0.05 \text{ s}^{-1}$

Photo 4 Microstructure of 50% compressing at 1150 and $\dot{\varepsilon} = 0.05 \text{ s}^{-1}$

Photo 5 Microstructure of 50% compressing at 1000 and $\dot{\varepsilon} = 0.5 \text{ s}^{-1}$

Photo 6 Microstructure of 50% compressing at 1050 and $\dot{\varepsilon} = 0.5 \text{ s}^{-1}$

Photo 7 Microstructure of 50% compressing at 1150 and $\dot{\varepsilon} = 0.5 \text{ s}^{-1}$

Photo 8 Microstructure of 50% compressing at 1000 and $\dot{\varepsilon} = 2.0 \text{ s}^{-1}$

Photo 9 Microstructure of 50% compressing at 1050 and $\dot{\varepsilon} = 2.0 \text{ s}^{-1}$

Photo 10 Microstructure of 50% compressing at 1150 and $\dot{\varepsilon} = 2.0 \text{ s}^{-1}$

Photo 11 Microstructure of hot compressed specimen to radial direction
at workpiece temp. = 1150 and die speed = 6 mm/s

Photo 12 Microstructure of hot compressed specimen to axial direction
at workpiece temp. = 1150 and die speed = 6 mm/s

List of Figures

- Fig. 1 Flow stress-strain curves in hot forming
- Fig. 2 Schematic view of the stress-strain curve of the steel
- Fig. 3 Schematic diagram of changes in the recrystallization structures
- Fig. 4 Schematic diagram of testing equipment
- Fig. 5 Diagram of experimental condition
- Fig. 6 Initial finite element mesh for the simulation
- Fig. 7 Flow chart for microstructure simulation
- Fig. 8 Stress-strain curves at the strain rate of 0.05 s^{-1}
- Fig. 9 Stress-strain curves at the strain rate of 0.1 s^{-1}
- Fig. 10 Stress-strain curves at the strain rate of 0.5 s^{-1}
- Fig. 11 Stress-strain curves at the strain rate of 2.0 s^{-1}
- Fig. 12 Strain dependence of activation energy (Q)
- Fig. 13 Strain dependence of strain rate sensibility (n)
- Fig. 14 Strain dependence of parameter $\ln(A)$
- Fig. 15 Stress-strain curves calculated in accordance with
the prediction and experimental data ($1000 \text{ }^\circ\text{C}$, $\dot{\epsilon} = 0.05 \text{ s}^{-1}$)
- Fig. 16 The graph of effective stress and strain hardening rate
- Fig. 17 Flow curves of experimental and predicted for $\dot{\epsilon} = 0.05 \text{ s}^{-1}$
- Fig. 18 Flow curves of experimental and predicted for $\dot{\epsilon} = 0.1 \text{ s}^{-1}$
- Fig. 19 Flow curves of experimental and predicted for $\dot{\epsilon} = 0.5 \text{ s}^{-1}$
- Fig. 20 Flow curves of experimental and predicted for $\dot{\epsilon} = 2.0 \text{ s}^{-1}$

Fig. 21 Comparison of load between simulation and experiment

Fig. 22 Distribution of retained strain

Fig. 23 Distribution of strain rate

Fig. 24 Distribution of recrystallized volume fraction

Fig. 25 Distribution of mean grain size

Fig. 26 Comparison of measured recrystallized volume fraction
and simulation results

Fig. 27 Comparison of measured grain size and simulation results

1.

1.1

가
가 . 가 가 ,
가
, , , , . 가
가
가 가
(annealing) 가 (stress)
.
(T), ($\dot{\epsilon}$), (σ)
가
가
.
(deformation resistance)
[1]. , 가
가 가 .
가 가 (T), ($\dot{\epsilon}$), (ϵ)
(dynamic recovery, DRV)
(dynamic recrystallization, DRX)

304 가 , (strain rate), (flow stress)

1.2

가 , ,
 , 가
[2-4,11].

Medina [5-8]

Zener-Hollomon

(peak strain)

가

. Shellar[9] 가

, Pietrzyk [10]

, Choi [11] Inconel 718

Venugppal [12-13] 가

304

, 가

. Barraclough [14] 304

, Towle [15]

304

316

· , Ryan [16] 304

· , Han

[17] 304

·

·

·

1.3

가

가

가

가

,

가

,

가

·

304

,

,

· 304

가

·

304

가

·

2. 가

가 (dislocation density)가

가 가 가

·
· 가

, 가

가

. Fig. 1

가

, 가

()

가

()

가

. Fig. 2

가

2.1

Fig. 3

2.2

가 가 가

가

[1-20]. 가

가 , (ϵ_c :

) ()

) ()가

Fig 3.

가 가

가 ,

,

,

A1

(peak stress)

가

가 ,

(steady state stress)

2.3

Fig. 3

가

(annealing)

2.4

가 .

Fig. 3

Fig. 3
가

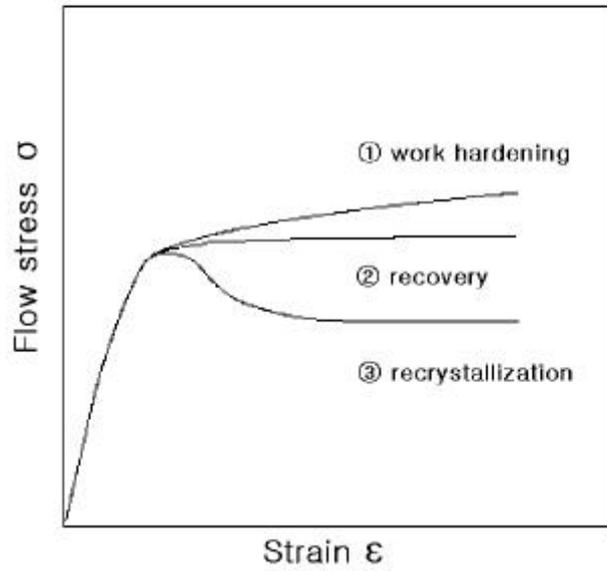


Fig. 1 Flow stress-strain curves in hot forming

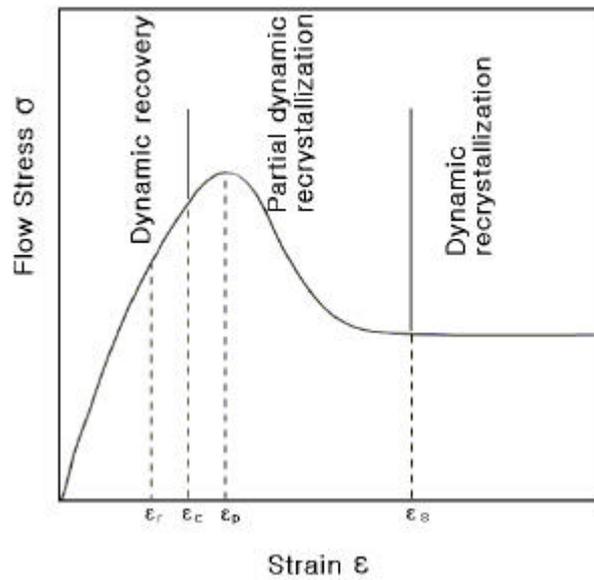


Fig. 2 Schematic view of the stress-strain curve of the steel

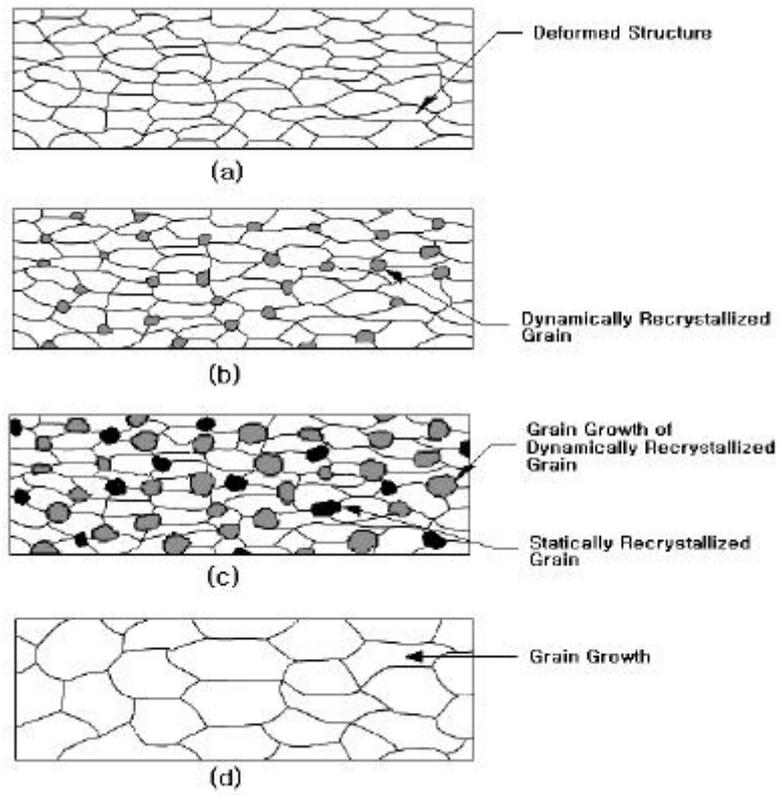


Fig. 3 Schematic diagram of changes in the recrystallization structures

3.

가

3.1

가

(Bauschinger effect)

가 (isotropic)

Von Mises

$$\text{(equilibrium equations) : } \frac{\sigma_{ij}}{x_j} = 0 \quad (1)$$

(compatibility conditions) :

$$\dot{\epsilon}_{ij} = \frac{1}{2} \left(\frac{u_i}{x_j} + \frac{u_j}{x_i} \right) \quad (2-a)$$

$$\text{: } \dot{\epsilon}_{ii} = \dot{\epsilon}_v = 0 \quad (2-b)$$

$$\text{(constitutive equations) : } \dot{\epsilon}_{ij} = \frac{3}{2} \frac{\dot{\epsilon}}{\sigma} \sigma_{ij}' \quad (3)$$

$$\bar{\sigma} = \sqrt{3/2} \{\sigma_{ij}' \sigma_{ij}'\}^{1/2}, \quad \dot{\bar{\epsilon}} = \sqrt{2/3} \{\dot{\epsilon}_{ij} \dot{\epsilon}_{ij}\}^{1/2}, \quad \sigma_{ij}'$$

$$\frac{\bar{\sigma}}{V}, \quad \frac{\dot{\bar{\epsilon}}}{S}, \quad S_f, \quad v_i$$

$$S_v, \quad T_i$$

$$n_j, \quad (4)$$

$$T_i, \quad v_i \quad \text{가} \quad (5)$$

$$T_i = \sigma_{ij} n_j \quad (4)$$

$$\pi = \int_V \frac{\bar{\sigma}}{\dot{\bar{\epsilon}}} dV - \int_{S_f} T_i v_i dS \quad (5)$$

(5)

$$\delta\pi = \int_V \frac{\bar{\sigma}}{\dot{\bar{\epsilon}}} \delta \dot{\bar{\epsilon}} dV + K \int_V \dot{\epsilon}_v \delta \dot{\epsilon}_v dV - \int_{S_f} T_i \delta v_i dS \quad (6)$$

3.2

$$K_1 T_{,ii} - \rho c \dot{T} + k^* \frac{\dot{\bar{\sigma}}}{\dot{\bar{\epsilon}}} = 0 \quad (7)$$

K_1 (thermal conductivity), k^*

0.85 0.95 . -

) (free surface)

(convection heat flux) :

$$q_n^c = h(T_a - T_s) \quad (8)$$

(radiation heat flux) :

$$q_n^r = \sigma \epsilon (T_a^4 - T_s^4) \quad (9)$$

, h , T_a , T_s

)

(conduction heat flux) :

$$q_n^d = h_{lub} (T_d - T_w) \quad (10)$$

(friction heat flux) :

$$q_n^f = m k_y v \quad (11)$$

h_{lub} , k_y , m

.

, , 가

(weak integral form)

$$\int_V (K_{1T,ij} - \rho c \dot{T} + k^* \frac{\dot{\epsilon}}{\sigma \epsilon}) \delta T dV = 0 \quad (12)$$

(13) ,

$$\int_V K_{1T,i} (T_{,i} \delta T)_{,i} dV - \int_V \rho c \dot{T} \delta T dV + \int_V k^* \frac{\dot{\epsilon}}{\sigma \epsilon} \delta T dV - \int_S K_{1T,i} \delta T_{,i} dV = 0 \quad (13)$$

(divergence theorem) (14)

$$\int_V K_{1T,i} \delta T_{,i} dV + \int_V \rho c \dot{T} \delta T dV - \int_V k^* \frac{\dot{\epsilon}}{\sigma \epsilon} \delta T dV - \int_{S_j} q_n \delta T dS = 0 \quad (14)$$

,

.

4.

4.1

304

Table 1. , (normalizing treatment)

1000 30
8mm, 12mm 가 .
(Thermecmaster) Photo. 1 ,

Fig. 4 . Fig. 5 가

5 /sec 가

1200 3 2 /sec 가 1000 ,
1050 , 1150 30 0.05 s⁻¹, 0.1 s⁻¹, 0.5
s⁻¹, 2 s⁻¹ 30%, 40%, 50% ,

가 .
(recrystallization volume
fraction)

가 (etching)

650 30 ,
(cold-mounting resin)

(polishing) .

60 cc 40cc
100 mA/mm² 30 (electrolytic
etching) . Photo. 2 10

4.2

1050 , 1150

0.8 mm/s, 3 mm/s, 6 mm/s

. 가

3 ,

3

4.3

가

Table 2

238

Fig. 6

187 , 160

Fig. 7

(X_{dyn})

($1 - X_{dyn}$)

X_{dyn}

, $1 - X_{dyn}$

(substructure)

X_{dyn}

$1 - X_{dyn}$

.

Table 1 Chemical compositions of stainless 304 and mechanical property

Element	C	Mn	Si	S	P	Ni	Cr	Mo	Cu	N	Co
Composition (wt%)	0.026	1.66	0.48	0.027	0.028	10.40	18.12	0.36	0.35	0.05	0.13
Mechanical property	Tensile strength		Elongation		Yield strength		Reduction of area		Hardness		
Value	720 N/mm ²		35.3 %		602 N/mm ²		68.5 %		HB 214		

Table 2 The conditions of process parameters for FE- simulation

Process Parameter	Value
Upper die velocity	6.0 (mm / s)
Friction coefficient	0.7
Initial temperature of work piece	1150
Initial temperature of dies	1150
Environment temperature	1150
Thermal conductivit of work piece	14.9 (J / m s K)
Thermal conductivity of dies	28.4 (J / m s K)
Heat capacity of work piece(c)	3.77×10^3 (kJ / m ³ K)
Heat capacity of die(c)	4.00×10^3 (kJ / m ³ K)



Photo 1 Testing equipment (Thermecmaster)

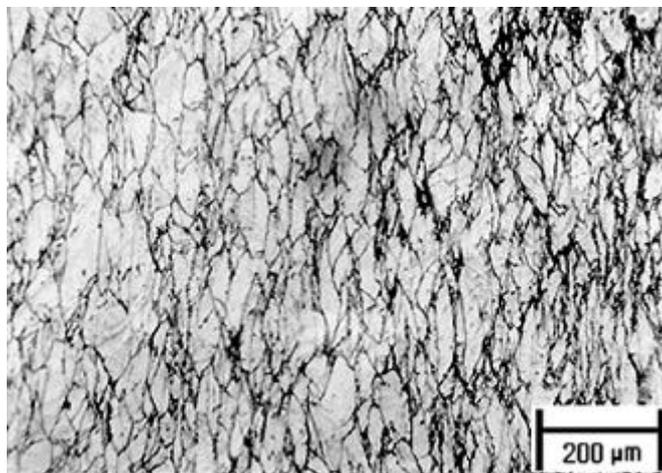


Photo 2 Microstructure of 50% compressing
at 1000 and $\dot{\epsilon} = 0.05 \text{ s}^{-1}$

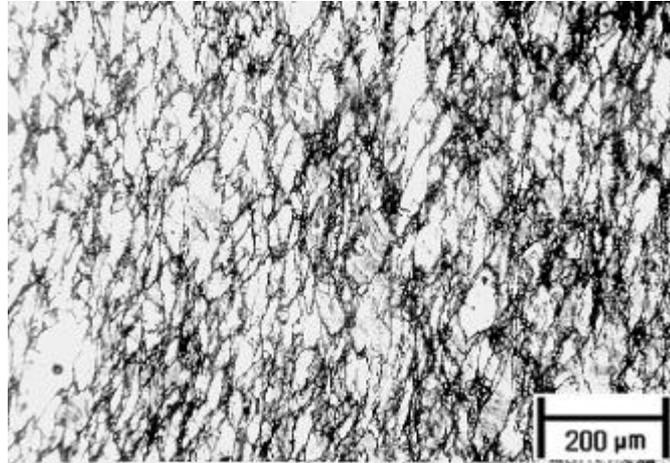


Photo 3 Microstructure of 50% compressing
at 1050 °C and $\dot{\epsilon} = 0.05 \text{ s}^{-1}$

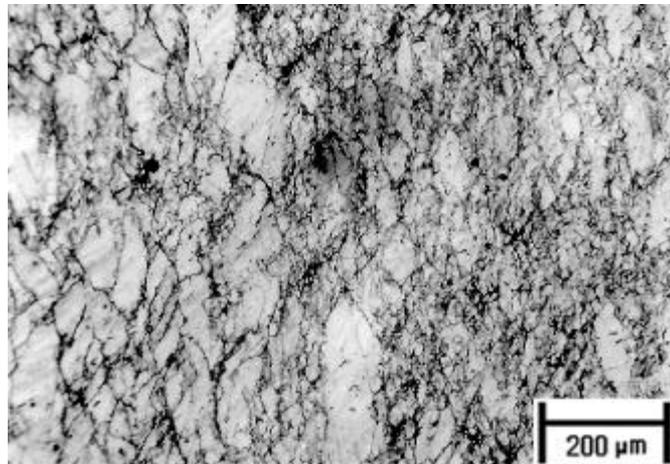


Photo 4 Microstructure of 50% compressing
at 1150 °C and $\dot{\epsilon} = 0.05 \text{ s}^{-1}$

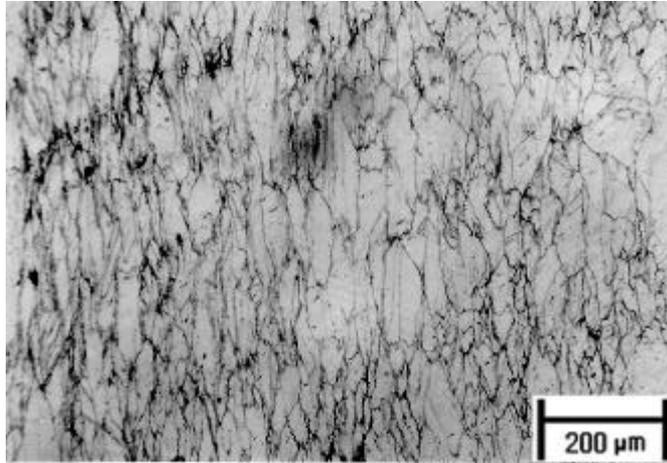


Photo 5 Microstructure of 50% compressing
at 1000 K and $\dot{\epsilon} = 0.5 \text{ s}^{-1}$

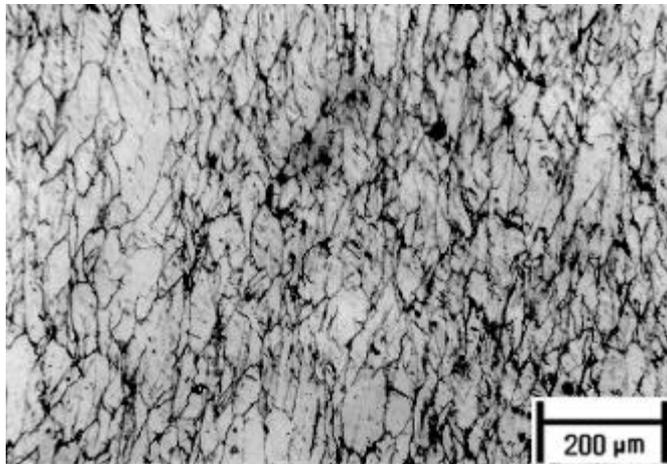


Photo 6 Microstructure of 50% compressing
at 1050 K and $\dot{\epsilon} = 0.5 \text{ s}^{-1}$

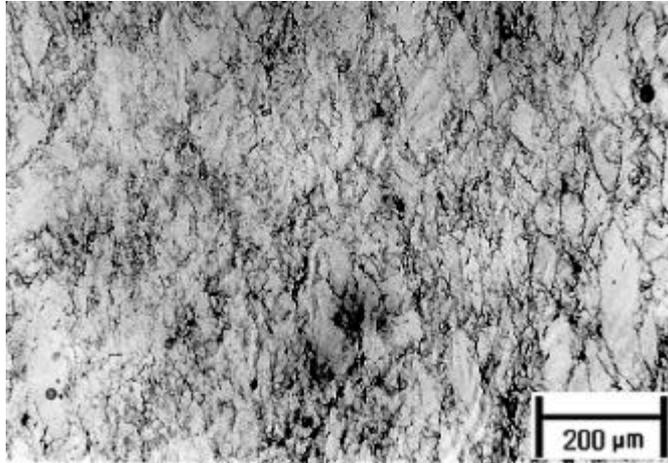


Photo 7 Microstructure of 50% compressing
at 1150 °C and $\dot{\epsilon} = 0.5 \text{ s}^{-1}$

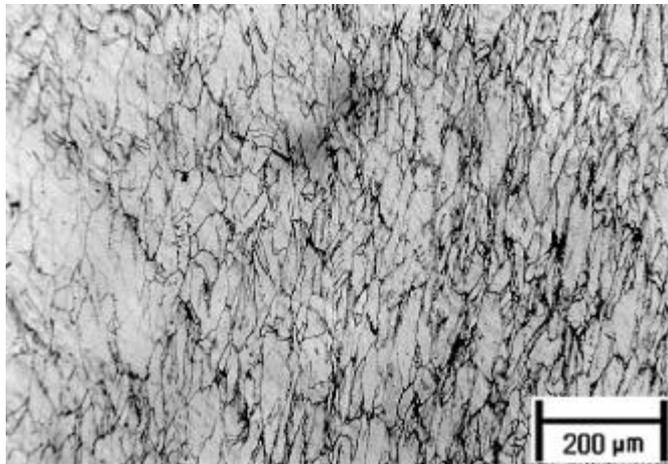


Photo 8 Microstructure of 50% compressing
at 1000 °C and $\dot{\epsilon} = 2.0 \text{ s}^{-1}$

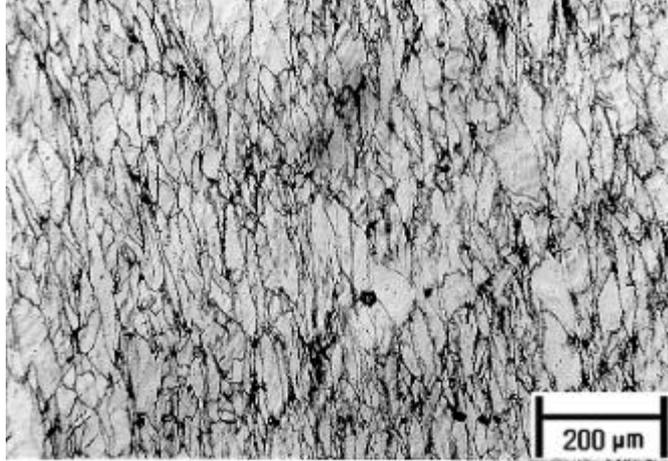


Photo 9 Microstructure of 50% compressing
at 1050 °C and $\dot{\epsilon} = 2.0 \text{ s}^{-1}$

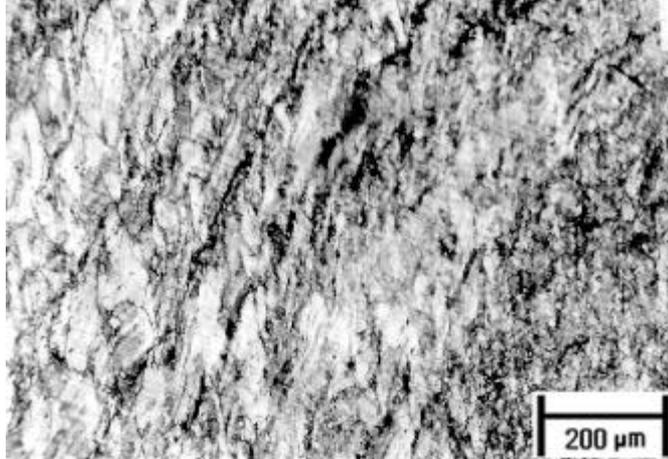


Photo 10 Microstructure of 50% compressing
at 1150 °C and $\dot{\epsilon} = 2.0 \text{ s}^{-1}$

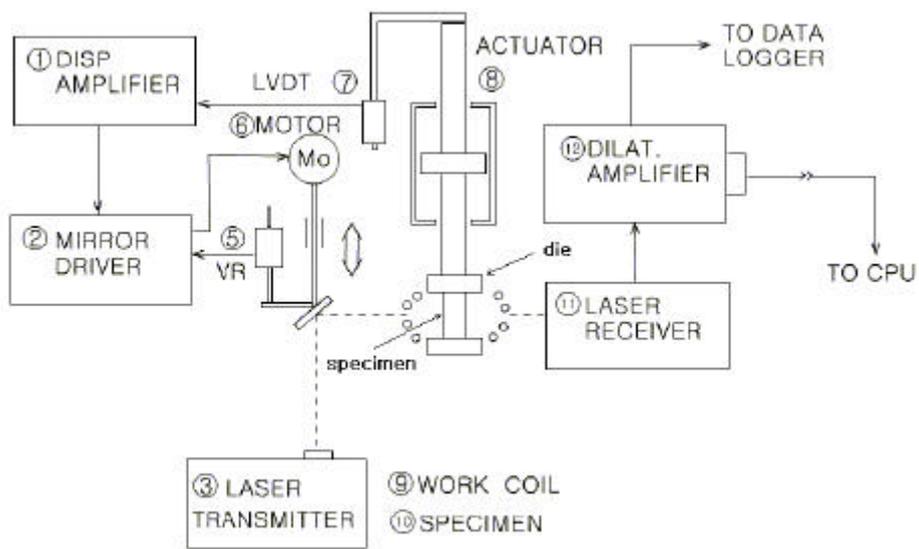


Fig. 4 Schematic diagram of testing equipment

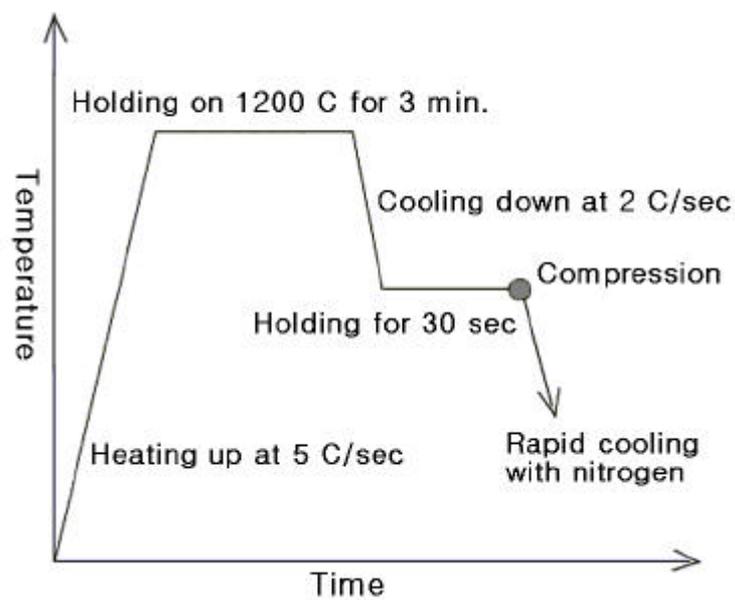


Fig. 5 Diagram of experimental condition

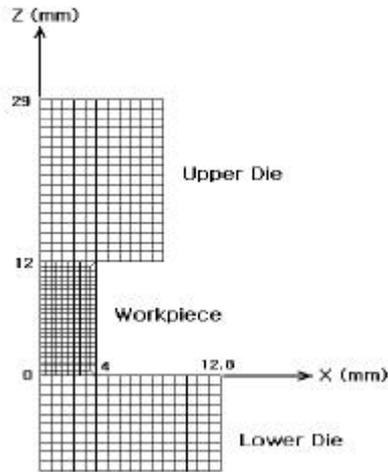


Fig. 6 Initial finite element mesh for the simulation

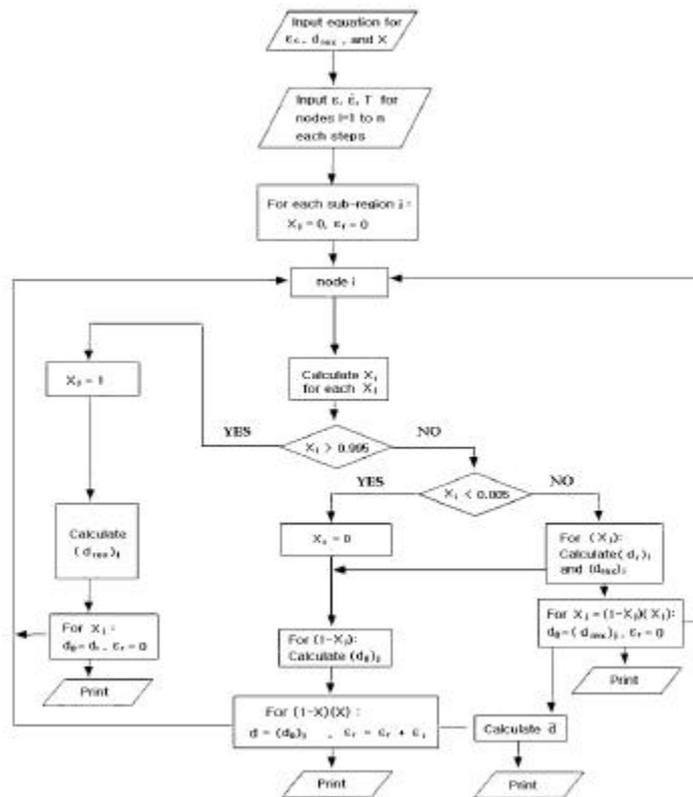


Fig. 7 Flow chart for microstructure simulation

5.

5.1

5.1.1

가

(T), ($\dot{\epsilon}$)

Arrhenius

가

[18].

Arrhenius

(power law),

(exponential law),

(hyperbolic-sin law)

$$\dot{\epsilon} = A_1 \sigma^n \exp(-Q/RT) \quad (15)$$

$$\dot{\epsilon} = A_2 \exp(\beta\sigma) \exp(-Q/RT) \quad (16)$$

$$\dot{\epsilon} = A_3 (\sinh(\alpha\sigma))^n \exp(-Q/RT) \quad (17)$$

가

가

n

가

가

가

n

304

Arrhenius

(σ(ε))
Zener Hollomon

Z

$$\sigma = \sigma(Z, \epsilon) \tag{18}$$

$$Z = \dot{\epsilon} \exp(Q/RT) \tag{19}$$

Z

$$[5]. \quad Q \tag{8.314}$$

, R

J/mol · K) .

Fig. 8 11
1000 , 1050 , 1150

0.05 s⁻¹, 0.1 s⁻¹, 0.5 s⁻¹, 2 s⁻¹

가

가

가 가

가 ,
가

가 가

가

가

가 . , 304

가 0.5 s^{-1} Fig. 8 Fig. 9 가

가 0.5 s^{-1} 가

가 가 Fig. 10 가 Fig. 11 Fig. 11 가
 2.0 s^{-1} Fig. 10(: 0.5 s^{-1}) 가
 Fig. 8 가

304 Arrhenius , Arrhenius
 (17) , (20)
 (20) n, R Q ,
 Fig. 12 Q ,

304 Q
 403.5 kJ/mol McQueen [16] 393 kJ/mol
 , Ni 170 kJ/mol ,
 294 kJ/mol , 336 kJ/mol 304

$$\ln(\sinh \alpha \sigma_p) = Q/nRT + C \quad (20)$$

Fig. 13 Fig. 14 Arrhenius n
A 가

(19) Zener-Hollomon

$$Z = \dot{\epsilon} \exp(Q/RT) = A [\sinh(\alpha\sigma)]^n \quad (21)$$

Zener-Hollomon

, Z
가 , ϵ_p
 σ_p , Z
, Z
, Z 가
가 가 , Z
가 가

$$\dot{\epsilon} = 1.586 \times 10^5 [\sinh(0.01\sigma)]^{4.35} \exp[-403.5 \text{ kJ} \cdot \text{mol}^{-1}/RT] \quad (22)$$

5.1.2

가

Avrami

[8].

$$\sigma = \sigma_e - \Delta\sigma \tag{23}$$

$$\sigma_e = B [1 - \exp(- C\varepsilon)]^m \tag{24}$$

$$\Delta\sigma = B' \left\{ 1 - \exp \left[- k \left(\frac{\varepsilon - \alpha\varepsilon_p}{\varepsilon_p} \right)^{m'} \right] \right\} \tag{25}$$

(24) 가 (25)

B, B', C, k

(,) , B, B' σ_p

$\sigma_p - \sigma_s$, .

$$B = \text{Lim}_{\varepsilon \rightarrow \varepsilon_p} \sigma_e \tag{26}$$

$$B' = \text{Lim}_{\varepsilon \rightarrow \infty} (\sigma_e - \sigma_s) \tag{27}$$

(26) (27) (23)

$$\sigma = \sigma_p [1 - \exp(- C\varepsilon)]^m - (\sigma_p - \sigma_s) \left\{ 1 - \exp \left[- k \left(\frac{\varepsilon - \alpha\varepsilon_p}{\varepsilon_p} \right)^{m'} \right] \right\} \tag{28}$$

C, m, k, m'

Z/A

, 304

1000
 Fig. 15
 0.05 s⁻¹
 가

$\alpha \epsilon_p$ ϵ_c Ryan [19,20]

α

Fig.

16 가
 (subgrain) 가

$$\alpha = \frac{\epsilon}{\epsilon_p} \quad \epsilon \leq \epsilon_c \quad (29-a)$$

$$\alpha = 0.7 \quad \epsilon > \epsilon_c \quad (29-b)$$

0.5 s⁻¹

가

0.5 s⁻¹

가

0.5 s⁻¹

0.5 s⁻¹

$$0.5 \text{ s}^{-1}$$

$$\sigma_p = 2.113 \dot{\epsilon}^{0.028} \exp(118.17 Q/RT) \quad (30-a)$$

$$\sigma_s = 1.607 \dot{\epsilon}^{-0.025} \exp(125.94 Q/RT) \quad (30-b)$$

$$\epsilon_p = 0.200 \dot{\epsilon}^{0.076} \exp(12.96 Q/RT) \quad (30-c)$$

$$C = 12.486 \dot{\epsilon}^{-0.260} \exp(-4.64 Q/RT) \quad (30-d)$$

$$m = 0.443 \dot{\epsilon}^{-0.006} \exp(-0.0003 Q/RT) \quad (30-e)$$

$$\Delta\sigma = 0 \quad (30-f)$$

$$0.5 \text{ s}^{-1}$$

$$\sigma_p = 1.467 \dot{\epsilon}^{0.278} \exp(145.74 Q/RT) \quad (31-a)$$

$$\sigma_s = 0.251 \dot{\epsilon}^{0.295} \exp(189.57 Q/RT) \quad (31-b)$$

$$\epsilon_p = 0.360 \dot{\epsilon}^{0.540} \exp(24.95 Q/RT) \quad (31-c)$$

$$C = 4.815 \dot{\epsilon}^{-0.963} \exp(-32.15 Q/RT) \quad (31-d)$$

$$m = 0.296 \dot{\epsilon}^{-0.510} \exp(-7.27 Q/RT) \quad (31-e)$$

$$k = 2.232 \dot{\epsilon}^{0.671} \exp(0.54 Q/RT) \quad (31-f)$$

$$m' = 4.091 \dot{\epsilon}^{0.443} \exp(-21.84 Q/RT) \quad (31-g)$$

. Fig. 17 20

가

$$(X_{dyn}) \quad (25)$$

$$X_{dyn} = 1 - \exp \left[-k \left(\frac{\varepsilon - \varepsilon_c}{\varepsilon_c} \right)^{m'} \right] \quad (32-a)$$

$$k = 0.028 \dot{\varepsilon}^{1.460} \exp(48.10 Q/RT) \quad (32-b)$$

$$m' = 1.171 \dot{\varepsilon}^{-0.194} \exp(1.10 Q/RT) \quad (32-c)$$

, k m' , ε_c

(22) (34)

$$d_{dyn} (\mu m) = 7.22 \dot{\varepsilon}^{0.22} \exp(-1.67 Q/RT) \quad (33)$$

$$d_{dyn} (\mu m) = 2.519 \times 10^5 [\sinh(0.01 \sigma)] \exp(-1.89 Q/RT) \quad (34)$$

가

$$\bar{D} = 46 (1 - X_{dyn}) + d_{dyn} \cdot X_{dyn} \quad (35)$$

5.2

0.8mm/s

가

3mm/s 6mm/s

. Photo. 11 12

1150

6mm/s

. Fig. 21

FEM

. Fig. 22 25

1150

6mm/s

. Fig. 22 Fig. 23

Fig. 24

. Fig. 25

가

가

가 가

Fig. 26 27

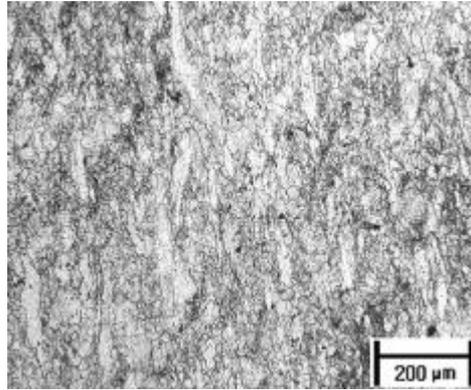
. Fig. 26

Fig. 27

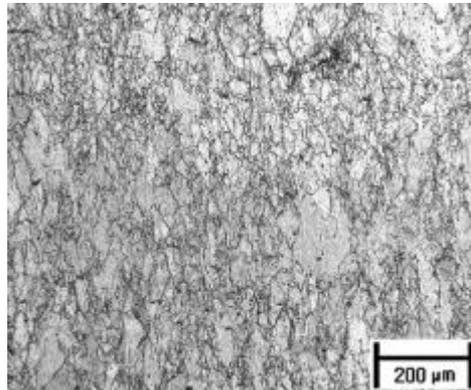
가

가

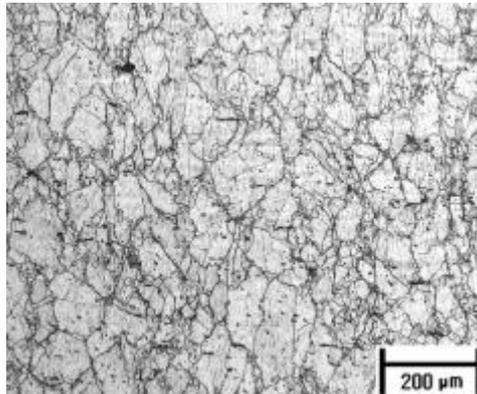
가 ,



(a) Central part ($\overline{D} = 9 \mu\text{m}$, $X_{\text{dyn}} = 90\%$)

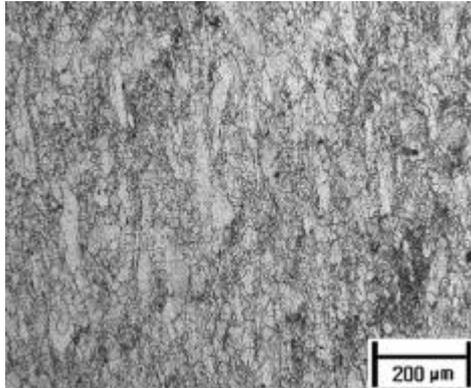


(b) 3 mm from center ($\overline{D} = 15 \mu\text{m}$, $X_{\text{dyn}} = 74\%$)

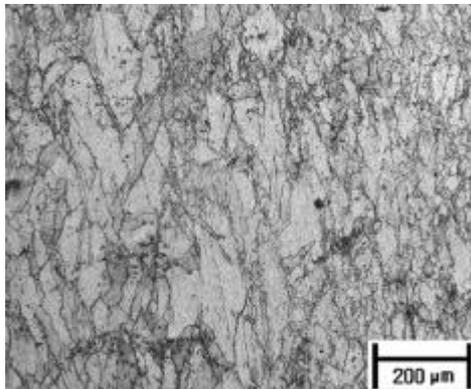


(c) 5.4 mm from center ($\overline{D} = 36 \mu\text{m}$, $X_{\text{dyn}} = 23\%$)

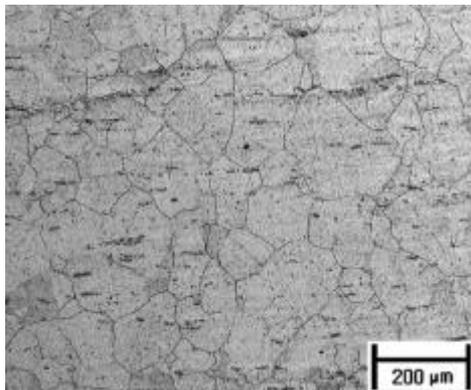
Photo 11 Microstructure of hot compressed specimen to radial direction
at workpiece temp. = 1150 and die speed = 6 mm/s



(a) Central part ($\overline{D} = 9 \mu\text{m}$, $X_{\text{dyn}} = 90\%$)



(b) 1.3 mm from center ($\overline{D} = 21 \mu\text{m}$, $X_{\text{dyn}} = 32\%$)



(c) 3 mm from center ($\overline{D} = 48 \mu\text{m}$, $X_{\text{dyn}} = 1\%$)

Photo 12 Microstructure of hot compressed specimen to axial direction
at workpiece temp. = 1150 and die speed = 6 mm/s)

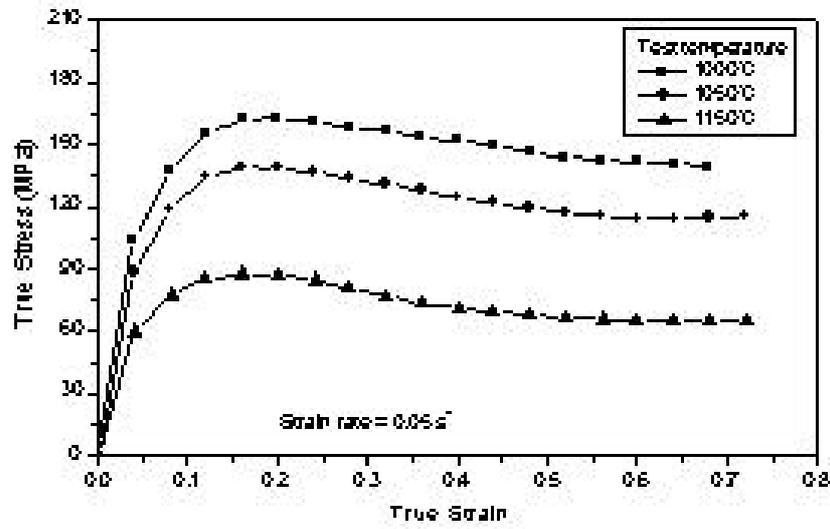


Fig. 8 Stress-strain curves at the strain rate of 0.05 s⁻¹

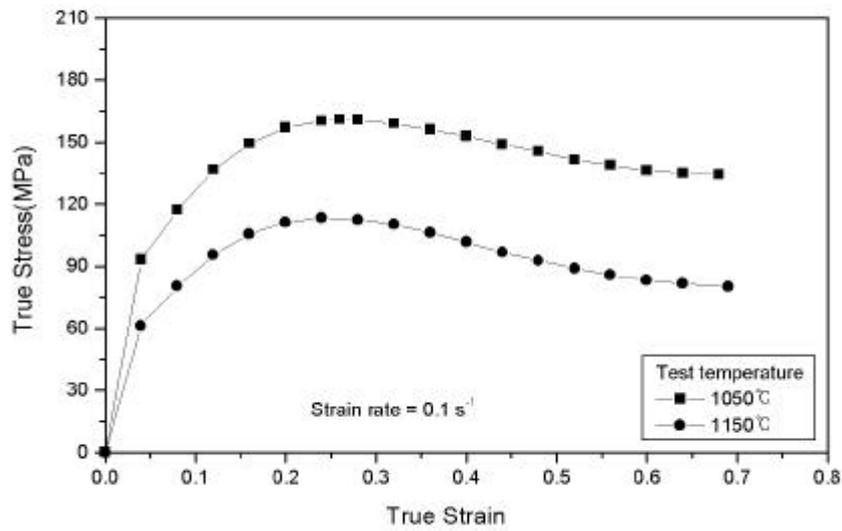


Fig. 9 Stress-strain curves at the strain rate of 0.1 s⁻¹

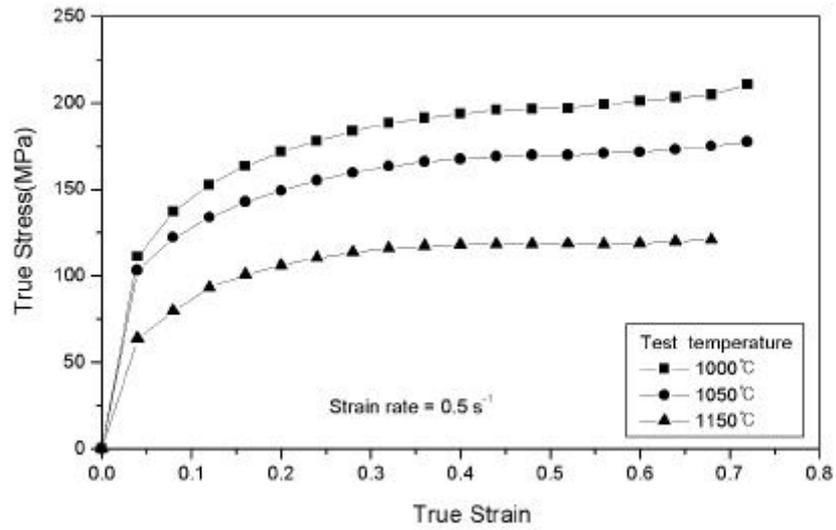


Fig. 10 Stress-strain curves at the strain rate of 0.5 s^{-1}

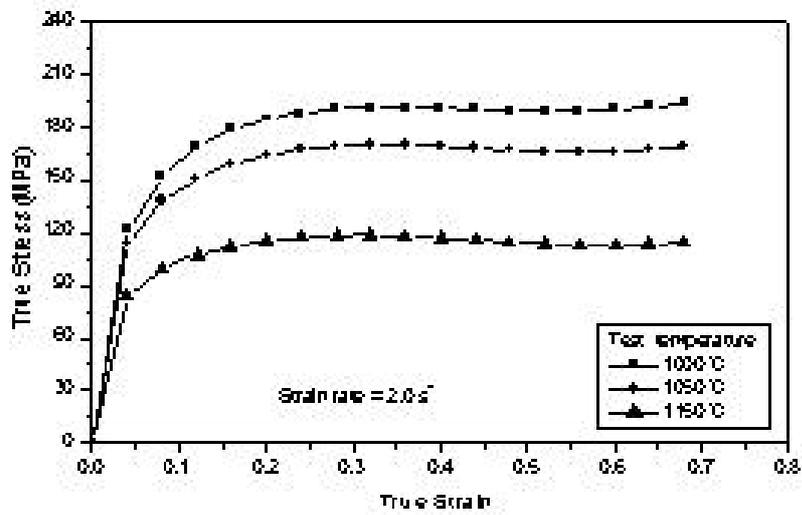


Fig. 11 Stress-strain curves at the strain rate of 2.0 s^{-1}

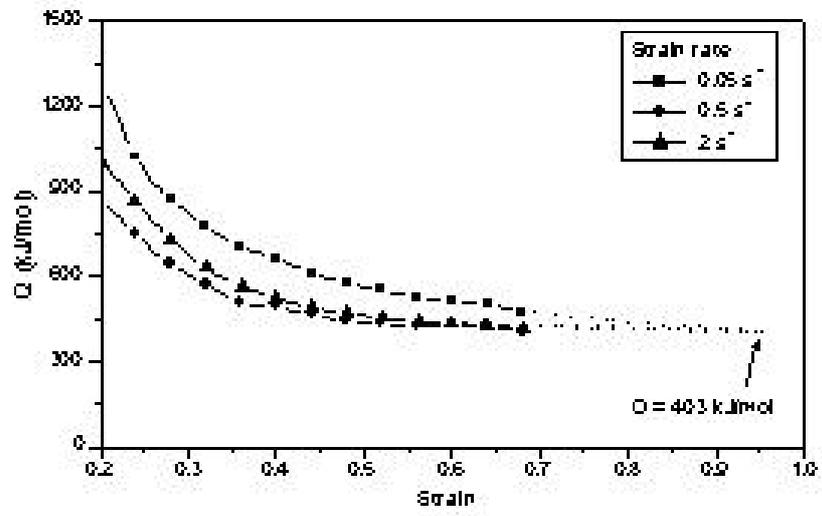


Fig. 12 Strain dependence of activation energy (Q)

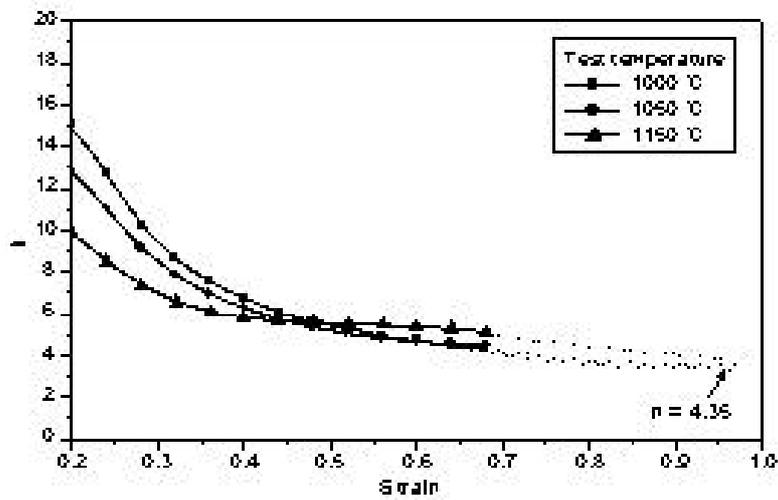


Fig. 13 Strain dependence of strain rate sensibility (n)

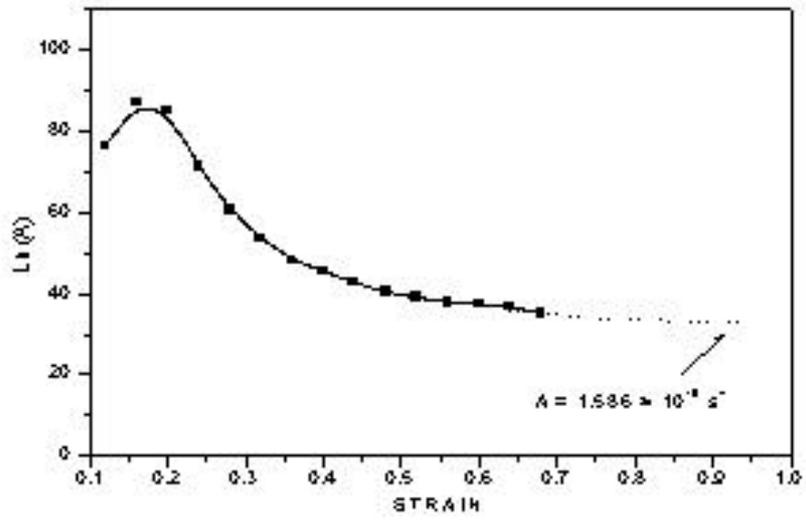


Fig. 14 Strain dependence of parameter $\ln(A)$

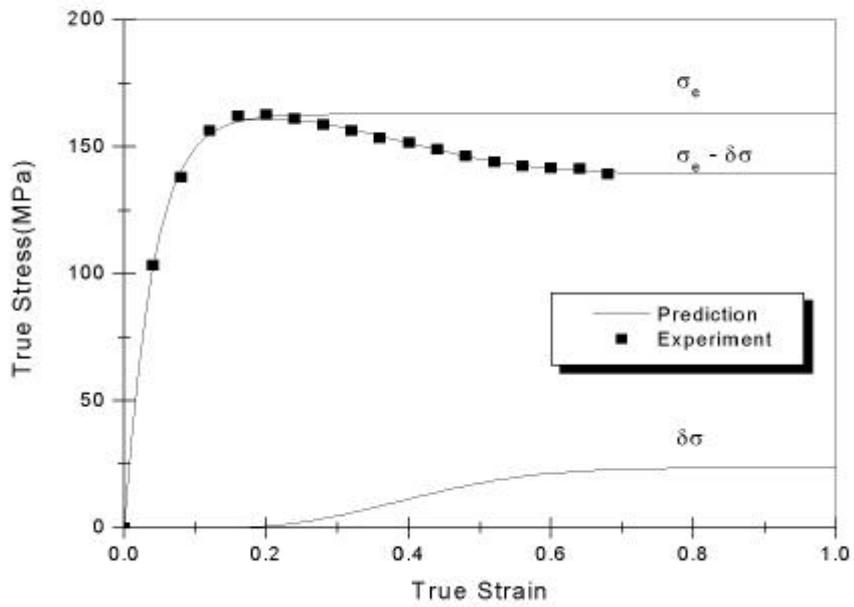


Fig. 15 Stress-strain curves calculated in accordance with the prediction and experimental data (1000 s^{-1} , $\dot{\epsilon} = 0.05 \text{ s}^{-1}$)

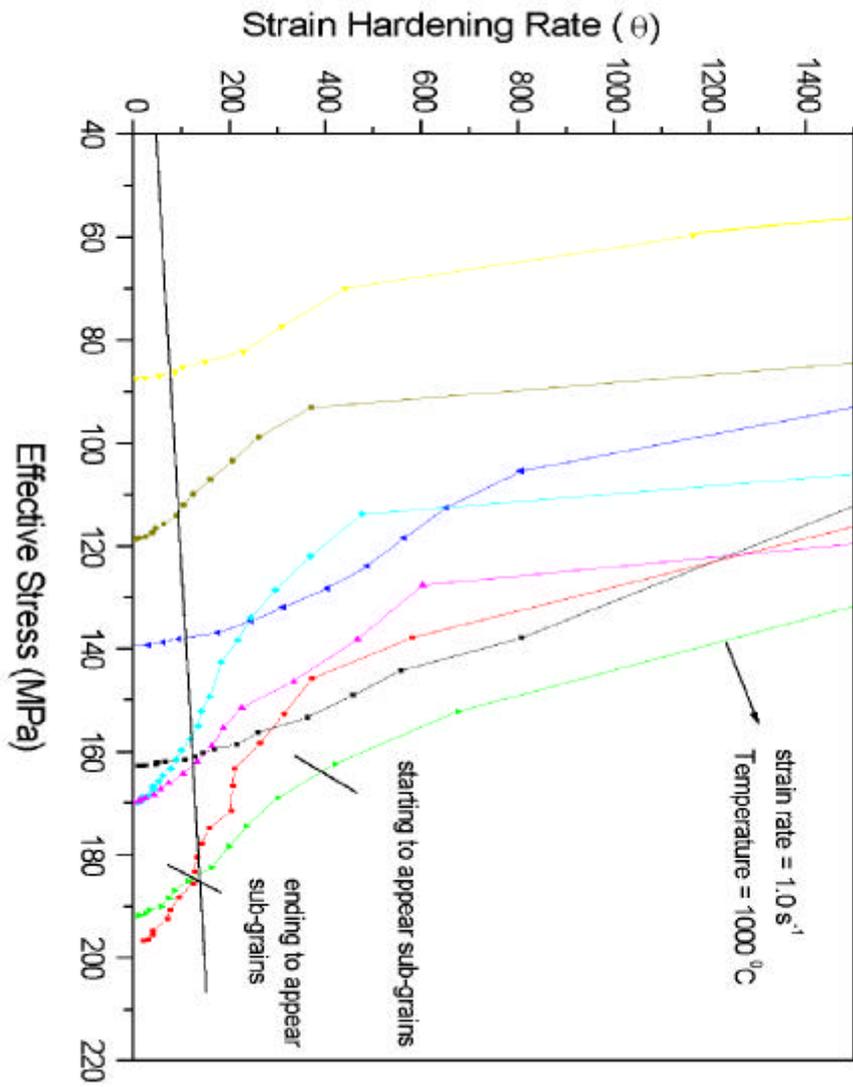


Fig. 16 The graph of effective stress and strain hardening rate

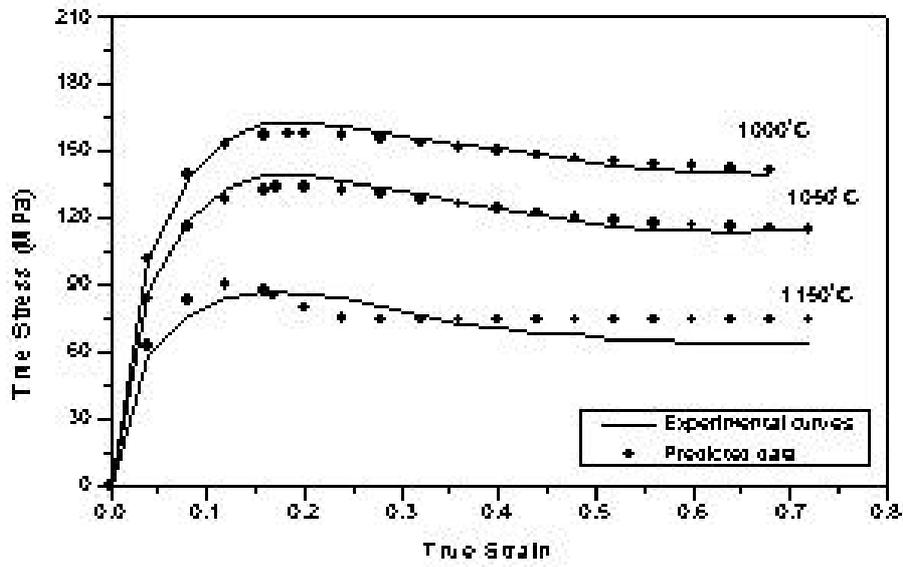


Fig. 17 Flow curves of experimental and predicted for $\dot{\epsilon} = 0.05 \text{ s}^{-1}$

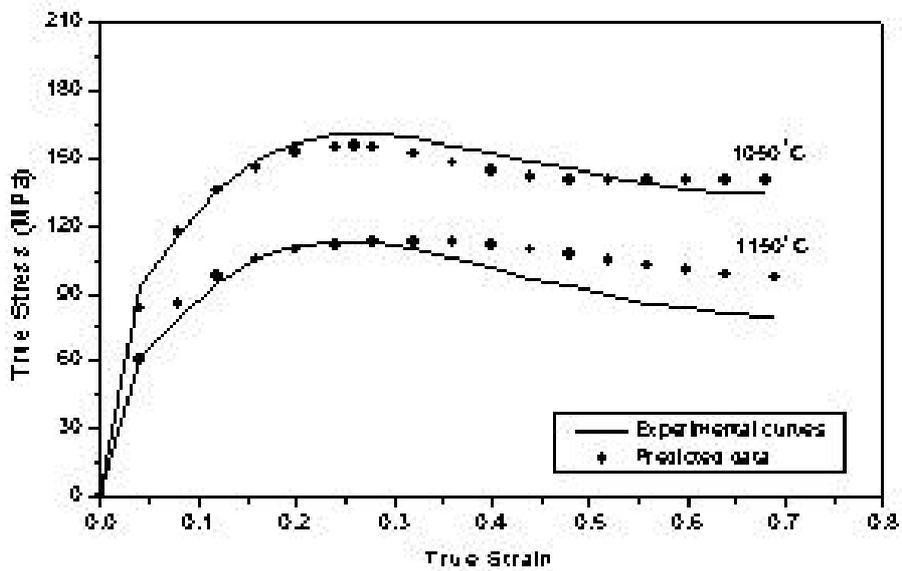


Fig. 18 Flow curves of experimental and predicted for $\dot{\epsilon} = 0.1 \text{ s}^{-1}$

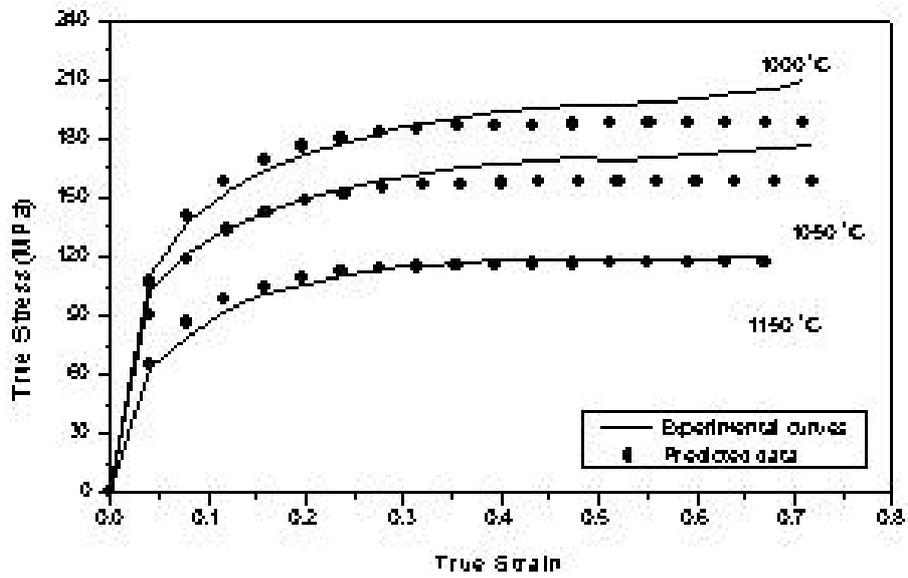


Fig. 19 Flow curves of experimental and predicted for $\dot{\epsilon} = 0.5 \text{ s}^{-1}$

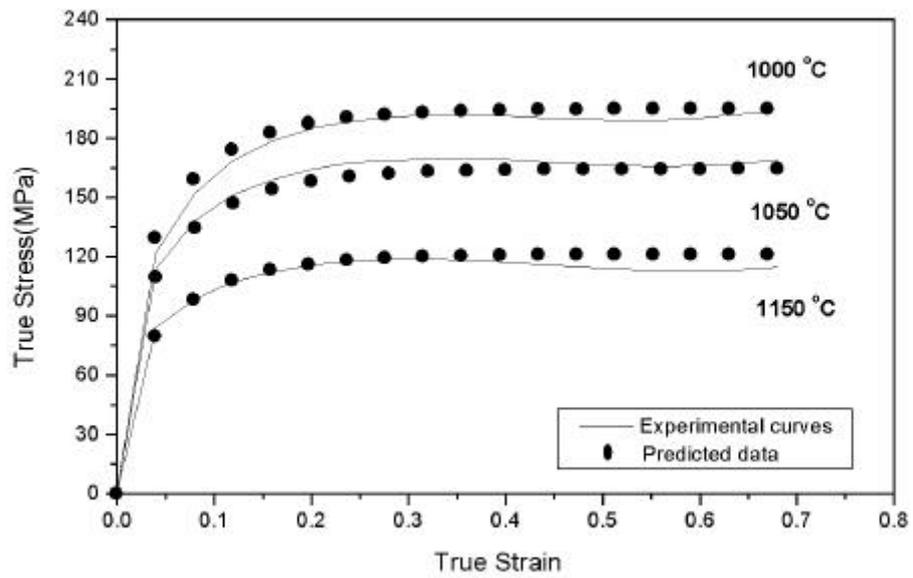


Fig. 20 Flow curves of experimental and predicted for $\dot{\epsilon} = 2.0 \text{ s}^{-1}$

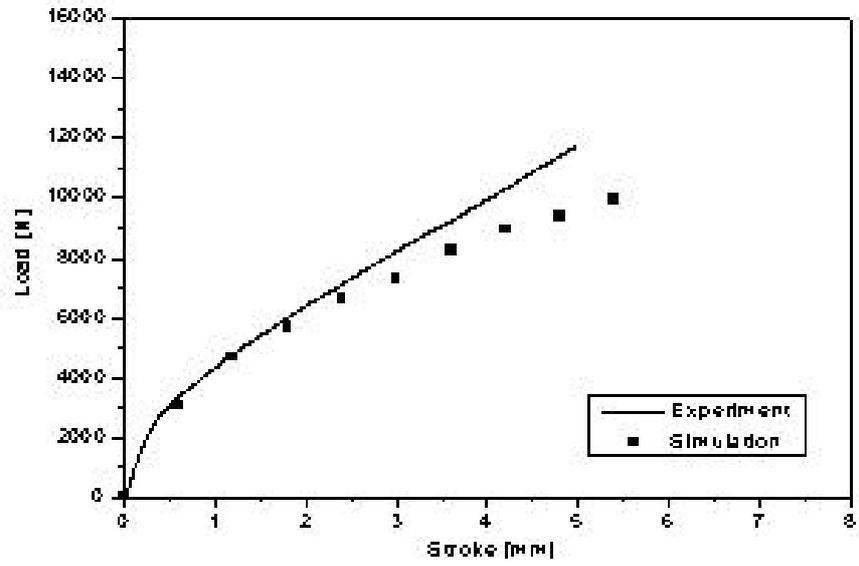


Fig. 21 Comparison of load between simulation and experiment

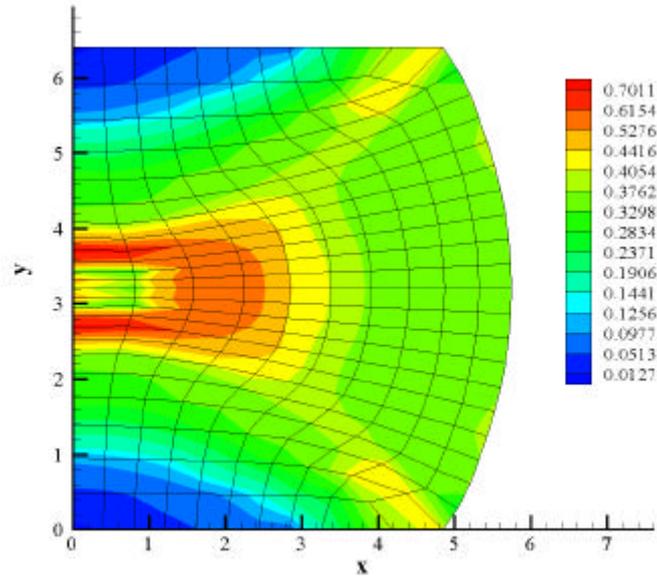


Fig. 22 Distribution of retained strain

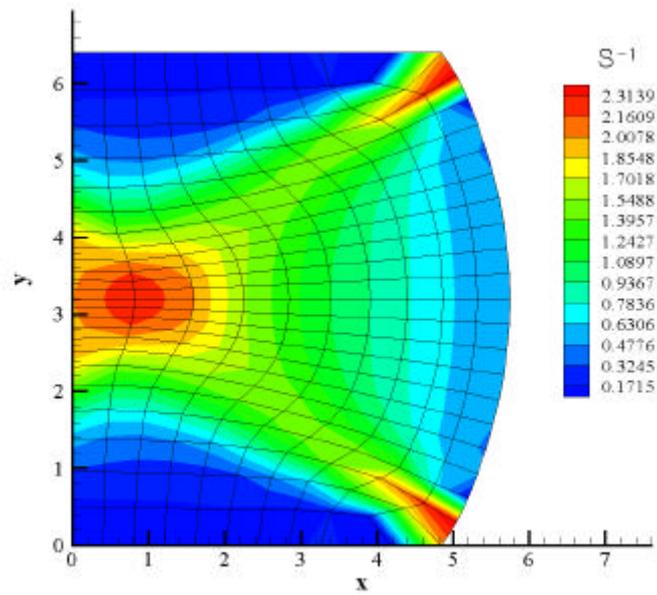


Fig. 23 Distribution of strain rate

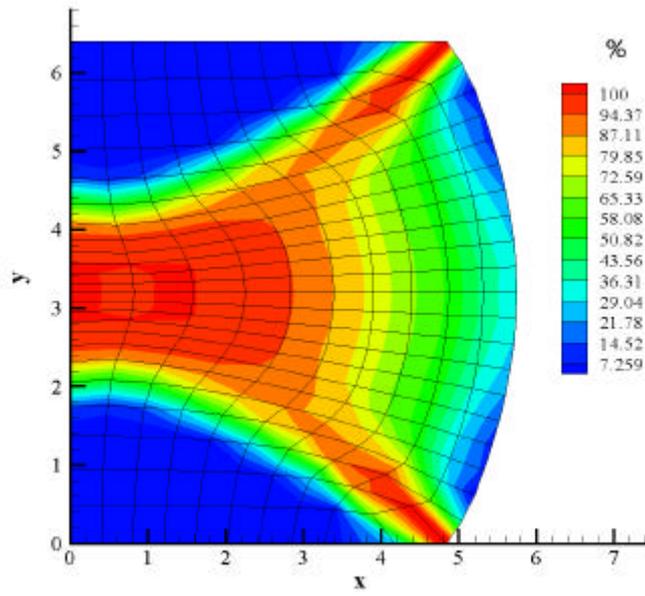


Fig. 24 Distribution of recrystallized volume fraction

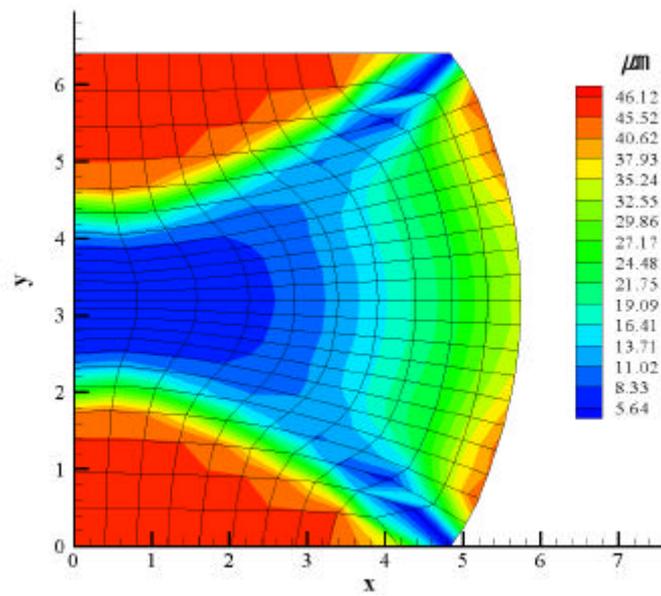
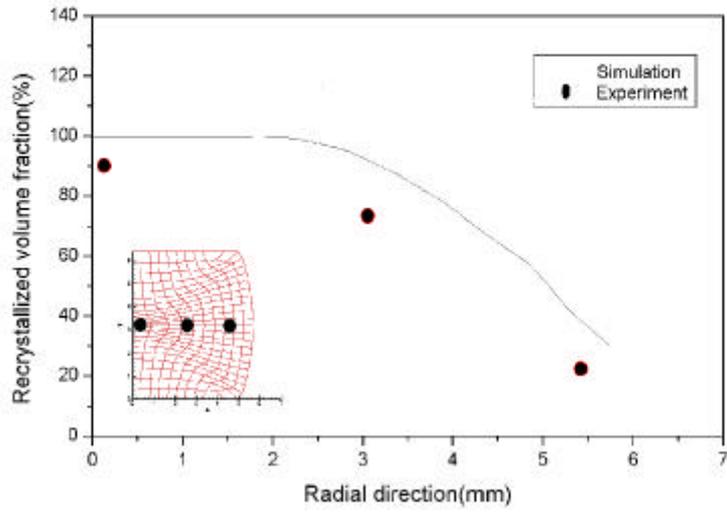
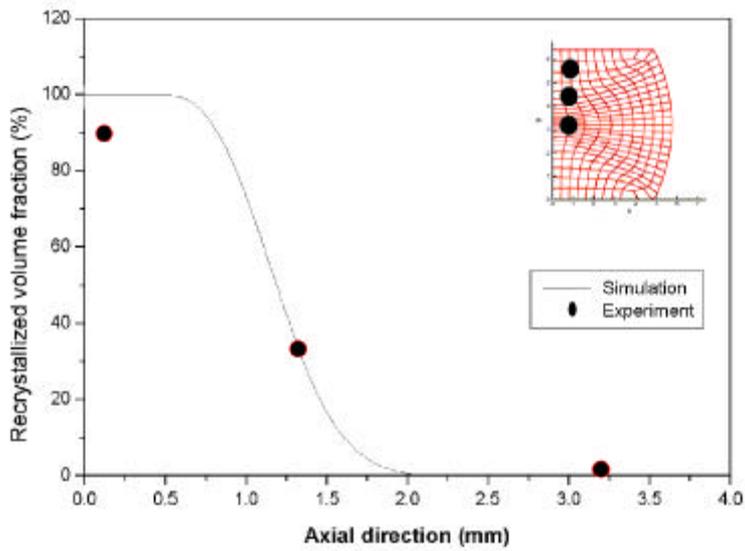


Fig. 25 Distribution of mean grain size

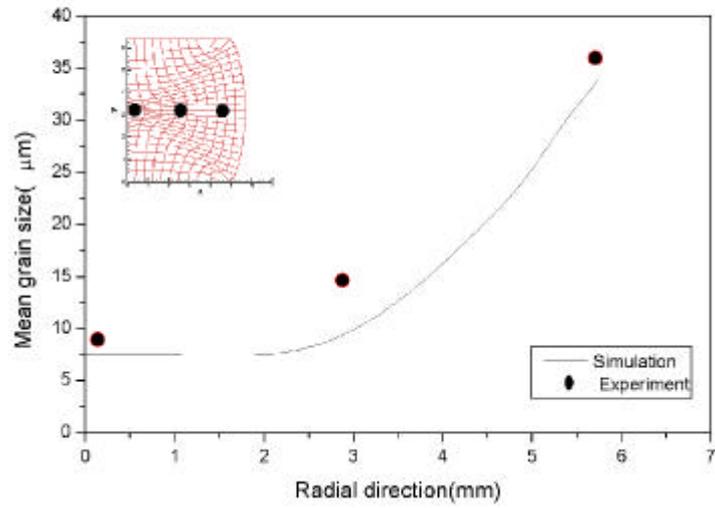


(a) Radial direction

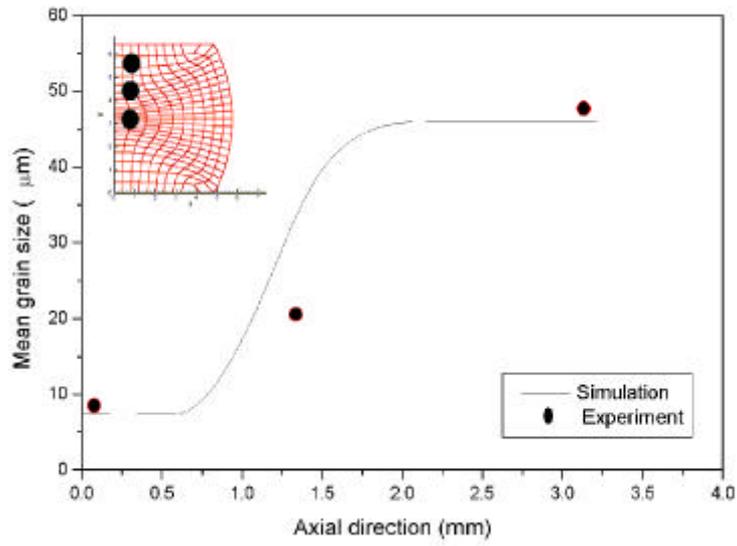


(b) Axial direction

Fig. 26 Comparison of measured recrystallized volume fraction and simulation results



(a) Radial direction



(b) Axial direction

Fig. 27 Comparison of measured grain size and simulation results

6.

304

, , ,

304

(1)

304

가

(2)

, ,

304

(3)

가

, 304

(4)

가
가

(5) 가 가

- [1] , , “ 가 STS304 ”, , Vol. 4, No. 4, pp. 46 54, 1990.
- [2] , , , “ Al-5wt%Mg ” 가 , Vol.8, No. 6, pp. 620 625, 1999.
- [3] Gangshu Shen, S.L.Semiatin, and Rajiv Shivpuri, “ Modeling microstructural development during the forging of waspaloy ”, Metall.Trans., Vol. 26A, pp. 1795 1803, 1995.
- [4] , , , , “ ”, 가 , Vol. 5, No. 4, pp. 305 319, 1996.
- [5] S.F.Medina, C.A.Hernandez, “ General expression of the Zener - Hollomon parameter as a function of the chemical composition of low alloy and microalloyed steels ”, Acta mater., Vol. 44, No. 1, pp. 137 148, 1996.
- [6] S.F.Medina, C.A.Hernandez, “ The influence of chemical composition on peak strain of deformed austenite in low alloy and microalloyed steels ”, Acta mater., Vol. 44, No. 1, pp. 149 154, 1996.
- [7] C.A.Hernandez, S.F.Medina, “ Modeling austenite flow curves in low alloy and microalloyed steels ”, Acta mater., Vol. 44, No. 1, pp. 155 163, 1996.
- [8] S.F.Medina, C.A.Hernandez, “ Modeling of the dynamic recrystallization of austenite in low alloy and microalloyed steels ”, Acta mater., Vol. 44, No. 1, pp. 165 171, 1996.
- [9] C.M.Shellars, “ The physical metallurgy of hot working ”, International conference on hot working and forming processes, Univ. of sheffield, pp. 3 15, 1979.

- [10] M.Pietrzyk, Z.Kedzierski, J.G.Lenard, "Finite element simulation of mechanical, thermal and structural phenomena in the hot rolling process", Numerical methods in industrial forming processes, ISBN 90 54 10 0877, pp. 749 754, 1992.
- [11] , , , , "Prediction of the behavior of dynamic recrystallization in inconel 718 during hot forging", 가 , '97 , pp. 220 223, 1997.
- [12] S.Venugopal, S.L.Manman, Y.V.R.K. Prasad, "Optimization of hot workability in stainless steel-type AISI 304L using processing maps", Metallurgical Transaction A, Vol. 23A, pp. 3093 3103, 1992.
- [13] S.Venugopal, S.L.Manman, Y.V.R.K. Prasad, "On the modelling of grain size during hot working of stainless steels type AISI 304 and 316", Journal of Materials Science Letters, Vol. 16, pp. 137 142, 1997.
- [14] D.R.Barraclough, C.M.Sellars, "Static recrystallization and restoration after hot deformation of Type 304 stainless steel", Metal Science, March-April, pp. 257 267, 1979.
- [15] D.J.Towle, T.Gladman, "Recrystallization of austenitic stainless steels after hot rolling", Metal Science, March-April, pp. 246 256, 1979.
- [16] N.D.Ryan, H.J.McQueen, "Dynamic softening mechanisms in 304 austenitic stainless steel", Canadian Metallurgical Quarterly, Vol. 29, No. 2, pp. 147 162, 1990.
- [17] , , , "Prediction on flow stress curves and microstructure of 304 stainless steel", 가 , Vol. 9, No. 1, pp. 72 79, 2000.
- [18] , , , , , , "304

”, , Vol. 35, No. 6, pp. 681
688, 1997.

[19] N.D.Ryan, H.J.McQueen, “ Hot deformation characteristics of worked
301 austenitic stainless steel ”, Proceedings of the 7th international
conference, Vol. 2, pp. 935 940, 1986.

[20] G.Carfi, C.Perdrix, D.Bouleau, C.Donadille, “ Microstructure evolution
of AISI 304L grade stainless steel during isothermal straining by hot
torsion ”, Proceedings of the 7th international conference, Vol. 2, pp.
929 934, 1986.

[21] , “ 3 - ”,
, 1993.

가

가

가

가

가